Dynamic Catalysis Multiscale Simulations for Nonoxidative Coupling of Methane Using Light and Heat

ACS Catalysis

pubs.acs.org/acscatalysis
Research Article

Dynamic Catalysis Multiscale Simulations for Nonoxidative Coupling of Methane Using Light and Heat

Juganta K. Roy, Mona Abdelgaid, Henrik Grönbeck, and Giannis Mpourmpakis*

Cite This: ACS Catal. 2025, 15, 1195−1205
Read Online

ACCESS | Metrics & More | Article Recommendations | Supporting Information

ABSTRACT: Methane (CH_4) activation and conversion under mild reaction conditions are a great challenge for the chemical industry. Photocatalysis is attractive for activating inert C−H bonds of CH_4 at room temperature. Specifically, photocatalytic nonoxidative coupling of CH_4 (NOCM) is a promising process to produce ethane (C_2-hydrocarbon) and H_2. Different oxide-based photocatalysts have been used for room-temperature NOCM, and TiO_2 is a potential photocatalyst with a bandgap that can capture photons in the UV region. However, a fundamental understanding of the NOCM mechanism on TiO_2 is still missing. Herein, we apply multiscale modeling, combining density functional theory (DFT) calculations with kinetic Monte Carlo (kMC) simulations to investigate the photocatalytic NOCM on a rutile TiO_2(110) surface. DFT calculations revealed that the photogenerated holes mediate the homolytic activation of CH_4 via the formation of methyl radicals with an activation barrier that is 70% lower than that of the conventional thermocatalytic route. The generated methyl radicals further recombine to form ethane. The detailed reaction pathway energetics investigated with DFT-based kMC simulations revealed that ethane can be formed at 315.15 K, but the dissociated hydrogens poison the catalyst surface. Further thermocatalytic simulations revealed that increasing the temperature by thermal heating (ca. 690.15 K) facilitated H_2 formation and catalyst regeneration. Importantly, we demonstrate how photo- and thermocatalytic modes can be combined, facilitating NOCM on TiO_2 and a route to enable dynamic catalysis simulations through multiscale modeling, opening alternative avenues in computational catalyst discovery.

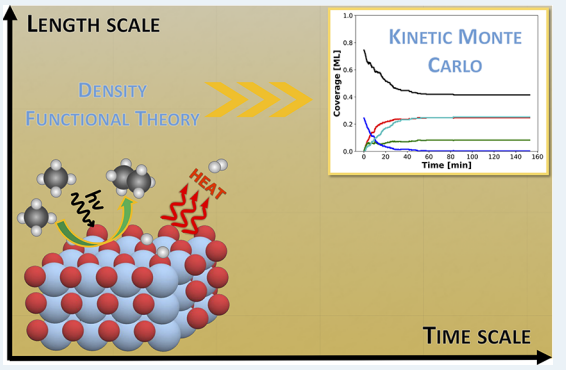

KEYWORDS: *photocatalysis, dynamic catalysis, nonoxidative coupling of methane, C−H bond activation, titanium dioxide, kinetic Monte Carlo, density functional theory*

INTRODUCTION

Technological advances in hydraulic fracking and increasing shale gas reserves make natural gas an attractive feedstock for producing valuable chemicals.[1−3] Methane (CH_4) is the major constituent of natural gas and its high H/C ratio makes CH_4 a valuable fuel source due to its efficient combustion capacity.[4] Additionally, CH_4 is a source of C_{2+} hydrocarbons, as well as of chemical reagents, such as carbon monoxide and hydrogen.[5,6] Conventionally, indirect CH_4 conversion to synthesis gas (CO and H_2), a feedstock for numerous value-added products, requires high reaction temperatures (973−1373 K) and pressures (10−40 atm).[6−8] This is because CH_4 possesses low electron affinity, low polarizability, and high C−H bond enthalpy (439 kJ mol^{-1}).[5,9] In contrast, direct conversion of CH_4 to higher C_{2+} hydrocarbons can be achieved via oxidative and nonoxidative coupling of CH_4 (OCM: $2CH_4 + O_2 \rightarrow C_2H_4 + H_2O$, NOCM: $2CH_4 \rightarrow C_2H_6 + H_2$, respectively),[10−14] however, both these routes are energy-intensive.[1,6,15]

Recent advances have been made in the thermocatalytic OCM to C_2 hydrocarbons (e.g., ethane and ethylene).[10,11,16] However, oxidation of the C_2 products to CO and CO_2 is unavoidable due to the high exothermicity of hydrocarbon combustion reactions, limiting the reaction selectivity. Alternatively, NOCM is one of the most selective routes to produce C_2 hydrocarbons. Nevertheless, NOCM is thermodynamically limited, requiring extremely high temperatures (>1273 K) to trigger CH_4 coupling, which leads to coke formation and rapid catalyst deactivation.[12,13] Different catalysts have been used for NOCM to increase the C_2 hydrocarbon yield and selectivity. For example, Xiao and Varma utilized Pt−Bi bimetallic catalysts for NOCM to ethane at high temperatures of 873−973 K, achieving a selectivity of over 90%.[17] Further, Guo et al. achieved a high CH_4

Received: July 19, 2024
Revised: December 19, 2024
Accepted: December 26, 2024

https://doi.org/10.1021/acscatal.4c04312
ACS Catal. 2025, 15, 1195−1205

conversion of 48.1% and a total hydrocarbon selectivity of 99% at a reaction temperature of 1363 K.[13]

Alternatively, photocatalytic NOCM is a promising and green approach (use of light as a source of energy compared to thermal heating from combustion) for CH_4 activation and conversion under mild conditions, driven by photonic energy.[7,18,19] Transition metal oxide (TMO) catalysts, with inherent Lewis acid−base properties, are promising photocatalysts for NOCM with strong lattice oxygen reactivity.[19−21] However, the lack of understanding of the NOCM mechanism at the molecular level on TMO hinders the design of optimal reaction systems for photocatalytic CH_4 conversion. CH_4 is a fully reduced molecule, hence its activation is driven solely by the oxidation reaction induced by the photogenerated holes.[7,22] Few studies have investigated the detailed mechanisms of photocatalytic NOCM to ethane.[21,23,24] Zhang et al. reported photocatalytic NOCM to ethane using heteroatom-engineered TiO_2, achieving 94.3% selectivity under mild conditions.[24] A photochemical looping strategy has been used to obtain a higher selectivity of methane coupling at ambient temperature with excellent stability.[23] Despite these significant findings, the activation of the C−H bond of CH_4 under light irradiation is not fully understood at the atomic level. It is important to note that photocatalytic CH_4 activation essentially differs from the common thermocatalytic activation.[25,26] Wei et al.[27] proposed that the hole-trapped lattice oxygen radical was responsible for CH_4 activation over the β-Ga_2O_3 photocatalyst under 254 nm light irradiation, which was also suggested on different metal oxide catalysts such as Ag-decorated ZnO[28] and $SrCO_3$/ $SrTiO_3$,[29] and others.[30] Most importantly, there is a lack of multiscale simulation strategies coupling fundamentally different activation processes, such as photocatalytic with thermal, at different scales, integrating molecular level mechanisms with overall kinetic behavior. Such simulation strategies would enable the prediction of dynamic catalytic behavior (i.e., catalytic events occurring under periodic operation), where the energy source can alternate (e.g., from light to thermal heating), enabling different catalytic pathways.

In this work, we combined density functional theory (DFT) calculations with kinetic Monte Carlo (kMC) simulations to investigate photocatalytic CH_4 activation and NOCM to ethane on rutile TiO_2. The results suggest that the photonic energy promotes CH_4 activation directly by the photogenerated hole polaron and offers kinetically favored NOCM to ethane at mild temperature, while an elevated temperature is needed for H_2 production and catalyst regeneration. Most importantly, our results underscore the importance of dynamic catalysis on hydrocarbon conversion and provide a pathway for such simulations.

COMPUTATIONAL METHODS

DFT Details. Spin-polarized plane-wave DFT calculations were performed using the projector augmented wave (PAW)[31] method, as implemented in the Vienna Ab initio Simulation Package (VASP 5.4.4).[32−34] The generalized gradient approximation (GGA) of the Perdew−Burke−Ernzerhof (PBE) functional was used.[35] van der Waals dispersion forces were considered using Grimme's D3 dispersion correction scheme[36] with Becke−Johnson damping.[37] In all DFT calculations, PAW pseudopotentials were used to model the interaction between the valence electrons and the core, whereas plane-wave basis sets with an energy cutoff of 400 eV were used to expand the Kohn−Sham orbitals. The valence electrons of the atoms were described as Ti ($3s^2 3p^6 4s^2 3d^2$), C ($2s^2 2p^2$), O ($2s^2 2p^4$), and H ($1s^1$). Due to the self-interaction error in DFT, photogenerated holes are delocalized in GGA calculations. There are two main methods to reduce the self-interaction error,[38−40] namely, hybrid functionals and DFT+U methods. As the hybrid functional calculations are expensive and time-consuming, we implemented the DFT+U method. In the DFT+U approach, a Hubbard-type correction (U) term was applied on the 3d orbitals of Ti and 2p orbitals of O. Specifically, U values of 6.3 and 8.5 eV were used for O 2p, whereas a U value of 5.0 eV was used for Ti 3d orbitals based on literature[41−43] and benchmarking calculations (Figures S1 and S2) to describe the hole polaronic states in TiO_2. The two different U values for the O 2p were used to stabilize two polarons on the surface by reducing the polaron−polaron interaction. We also performed the HSE06[44] single-point calculations on some key elementary steps to probe the accuracy of DFT+U (Table S1) and observed similar activity trends.

The (110) surface of rutile TiO_2 was modeled with a (3 × 2) periodically repeated slab with four O−Ti−O layers, consisting of 144 atoms. Additionally, an 18 Å vacuum layer between the slabs was utilized to reduce interaction between slabs. The Brillouin zone integration was sampled with a Γ centered (3 × 2 × 1) Monkhorst−Pack k-mesh. Self-consistent DFT energies were converged to 10^{-5} eV and all of the atoms were allowed to relax until the forces were less than 0.05 eV/Å with Gaussian smearing (σ = 0.2 eV). The climbing image nudged elastic band (CI-NEB)[45] and dimer methods[46] were used to optimize the transition state (TS) structures, with a force criterion of at least 0.05 eV/Å. All TSs were confirmed with the existence of a single imaginary frequency along the reaction coordinate.[47]

According to previous studies, a hydroxy group[48,49] or a fluorine (F) atom[50] can be used as an electron-withdrawing group to inject a hole polaron into the surface. Herein, photogenerated hole polarons were modeled either by removing an electron[42,48,49,51,52] from the periodic system or introducing a F atom[50] as an electron acceptor at the bottom of the slab. In the former approach, the charge is balanced by introducing a neutralizing jellium background charge. The bottommost two O−Ti−O layers were fixed for the positively charged systems, whereas all four O−Ti−O layers were relaxed for systems with the extra F atom. We compared the energetics for all the elementary steps using the two different hole polarons formation approaches and found that both methods resulted in the same activity trend, as shown in Figures S3, S5, and S6. The localization of the hole polaron was further confirmed by plotting the spin density distribution and Bader charges in the positively charged and F-added systems. For the positively charged system, the stability of polaron is computed according to the following relation:[41,53]

$$E_{\text{bind}}^{\pm} = E_{\text{polaron}}^{(N\mp1)} - E_{\text{perfect}}^{(N\mp1)}$$

where the plus in $E_{\text{bind}}^{\pm}$ corresponds to electron removal (hole polaron) and the minus sign corresponds to electron addition (electron polaron). E_{polaron} and E_{perfect} are the total energies of the distorted system (polaron geometry) and undistorted system, respectively. The number of electrons in the system is given in parentheses, with N corresponding to the neutral system. A negative $E_{\text{bind}}^{\pm}$ indicates an energy gain and a stable (self-trapped) polaron. In our DFT+U calculations, the first

https://doi.org/10.1021/acscatal.4c04312
ACS Catal. 2025, 15, 1195−1205

and second hole polaron formation energies for the positively charged $TiO_2(110)$ surface are −0.18 and −0.74 eV, respectively. Both polarons are localized on the O_{2c} of the rutile (110) surface.

Gibbs free energies (G) are reported for thermocatalytic NOCM pathways at 1240 K and calculated using statistical thermodynamics as per the formula in the equation:[54]

$$G = E + \mathrm{ZPE} + \int C_p \mathrm{d}T - TS$$

where ZPE is the zero-point energy, C_p is the heat capacity, S is the entropy, T is the temperature, and E is the total electronic energy of each system. The vibrational modes of only the adsorbates were factored into the free energy calculations. Enthalpic and entropic contributions of gas phase CH_4 and H_2 molecules were calculated with the ideal gas approximation, whereas the enthalpy and entropy of adsorbed and transition states were computed with the harmonic oscillator approximation.[55]

kMC Details. The reaction mechanism and kinetic parameters from the DFT calculations of the positively charged TiO_2 system were fed into kMC simulations. This pathway was chosen according to the favored reaction energy (−0.42 eV) of the first methane dissociation step over the F-added system (−0.03 eV). The applied kMC model is based on the MonteCoffee software,[56] which implements the first reaction method (FRM).[57] All possible reaction events are defined and stored in an event list. This event list stores the time of occurrence of each event and the site where the events proceed. Given the current (α) and future (β) states of the system, the events in the FRM are executed chronologically based on randomly generated time of occurrence as follows, and the event list is updated after each simulation step:

$$t_{\beta\alpha} = t - \frac{\ln(u)}{W_{\beta\alpha}}$$

where $t_{\beta\alpha}$ is the time when the event occurs, t is the current simulation time, $W_{\beta\alpha}$ is the reaction rate constant for the transition from state α to state β, and u is a random uniform number on the unit interval [0,1[. If an event is enabled, the first process in the list with the lowest $t_{\beta\alpha}$ is executed, and then the event list and the simulation time are updated accordingly. To enhance the performance and reduce the number of time evaluations, it is assumed that the executed events modify the lattice locally and only nearby events are affected. The TiO_2 surface is modeled using periodic boundary conditions with a 2D (20 × 20) supercell composed of two types of active sites, corresponding to Ti_{5c} and O_{2c} sites, for a total of 400 active sites. A nearest neighbor list is also constructed, which defines the sites' connectivity and which events are possible. For surface reactions, the forward and backward reaction rate constants follow the Eyring equation:

$$k_{\mathrm{frd}} = \frac{q_{\mathrm{vib}}^{\mathrm{TS}}}{q_{\mathrm{vib}}^{\mathrm{R}}} \times \frac{k_B T}{h} \times \exp\left(\frac{-E_{\mathrm{frd}}}{k_B T}\right)$$

$$k_{\mathrm{bwd}} = \frac{q_{\mathrm{vib}}^{\mathrm{TS}}}{q_{\mathrm{vib}}^{\mathrm{P}}} \times \frac{k_B T}{h} \times \exp\left(\frac{-E_{\mathrm{bwd}}}{k_B T}\right)$$

where q_{vib} is the vibration partition function of the reactants (forward reaction) or products (backward reaction) and the transition state, k_B is the Boltzmann constant, T is the temperature, h is the Planck constant, E_{frd} is the activation barrier in the forward reaction step, and E_{bwd} is the activation barrier in the backward reaction step. The identity $E_{\mathrm{frd}} - E_{\mathrm{bwd}} = \Delta E_{\mathrm{rxn}}$ must hold. For surface reactions involving gaseous species (Eley−Rideal reactions), the rotational and translational partition functions are accounted for using standard statistical mechanics as follows:

$$k_{\mathrm{frd}} = \frac{q_{\mathrm{vib}}^{\mathrm{TS}}}{q_{\mathrm{vib}}^{\mathrm{gas}} q_{\mathrm{rot}}^{\mathrm{gas}} q_{\mathrm{trans}}^{\mathrm{gas}}} \times \frac{pA}{\sqrt{2\pi m k_B T}} \times \exp\left(-\frac{E_{\mathrm{frd}}}{k_B T}\right)$$

where p is the pressure, A the effective area of the reaction site, and m is the mass of the gas species. It should be noted that $q_{\mathrm{rot}}^{\mathrm{TS}}$ and $q_{\mathrm{trans}}^{\mathrm{TS}}$ are assumed to be 1. The vibrational (q_{vib}), rotational (q_{rot}), and translational (q_{trans}) partition functions are calculated from the harmonic approximation using

$$q_{\mathrm{vib}}^{\mathrm{sur}}(T, \nu_i) = \prod_i \frac{\exp\left(-\frac{h\nu_i}{2k_B T}\right)}{1 - \exp\left(-\frac{h\nu_i}{k_B T}\right)}$$

$$q_{\mathrm{rot}}^{\mathrm{linear}}(T) = \frac{8\pi^2 I k_B T}{\sigma h^2} \quad \text{for molecular } H_2 \text{ (linear molecule)}$$

$$q_{\mathrm{rot}}^{\mathrm{nonlinear}}(T) = \frac{\sqrt{\pi I_a I_b I_c}}{\sigma} \times \left(\frac{8\pi^2 k_B T}{h^2}\right)^{3/2}$$

for molecular CH_4 and C_2H_6 (nonlinear molecules)

$$q_{\mathrm{trans}}(T) = A\frac{2\pi m k_B T}{h^2}$$

where ν_i is the vibrational frequency, I (I_a, I_b, I_c) are principal moments of inertia of the molecule in vacuum, and σ is the symmetry number of the molecule. For nonactivated adsorption where $E_{\mathrm{frd}} = 0$, the forward rate constant is obtained from collision theory:

$$k_{\mathrm{ads}} = \frac{pA}{\sqrt{2\pi m k_B T}}$$

Desorption rate constant is computed considering the equilibrium constant (K_{eq}):

$$k_{\mathrm{des}} = \frac{k_{\mathrm{ads}}}{K_{\mathrm{eq}}}$$

$$K_{\mathrm{eq}} = \frac{q_{\mathrm{vib}}^{\mathrm{ads}}}{q_{\mathrm{vib}}^{\mathrm{gas}} q_{\mathrm{rot}}^{\mathrm{gas}} q_{\mathrm{trans}}^{\mathrm{gas}}} \times \exp\left(-\frac{\Delta E}{k_B T}\right)$$

where ΔE is the energy of adsorption.

The catalyst light irradiation event is modeled as a first-order reaction:[58,59]

$$TiO_2 + h\nu \xrightarrow{k} e^- + h^+ + TiO_2$$

where the rate is governed by the intensity of the UV light beam, which is assumed to remain constant throughout the kMC simulation. The rate constant, k, for the light irradiation event, was calculated to be 1.24×10^{-3} s^{-1}, based on the work of Thampi et al.,[60] who studied the photoactivation of CH_4 at room temperature on TiO_2 supported on MoO_3, using an incident light flux of 5.3×10^{-4} Einstein/h.

https://doi.org/10.1021/acscatal.4c04312
ACS Catal. 2025, 15, 1195−1205

To perform the simulations under experimental reaction conditions, the temperature was set to 315.15 K. The kinetics of the photocatalytic NOCM reaction were explored under 0.25 ML CH_4 coverage according to Thampi et al.[60] The turnover frequency (TOF) for C_2H_6 formation is calculated as the number of formed C_2H_6 molecules divided by the total number of Ti and O surface sites (N_{sites}) and simulation runtime (t_{kMC}),

$$\mathrm{TOF}(C_2H_6) = \frac{N_{form}^{C_2H_6}}{N_{sites} \times t_{kMC}}$$

The convergence of surface species coverage with respect to time is monitored to ensure that steady-state conditions have been reached.

RESULTS AND DISCUSSION

Activation of the First CH_4 Molecule. As noted, the NOCM involves the adsorption and activation of two CH_4 molecules, followed by C−C coupling to produce ethane. We started our investigation with the thermocatalytic adsorption and activation of the first CH_4 molecule on a rutile TiO_2 (110) surface. Though the anatase polymorph of TiO_2 exhibits higher photocatalytic activity compared to rutile, the abundance and well-established surface science protocol of rutile (110) along with the thermodynamic stability of the facet made it a preferred option for fundamental photocatalysis studies.[61] Additionally, the bandgap of rutile (3.0 eV) is lower than that of anatase (3.2 eV), enabling rutile to be effective in visible light.[62,63] In general, CH_4 weakly adsorbs on metal oxides and its activation is mainly governed by the inherent Lewis acid−base properties of the active, metal−oxygen site pair.[64−66] On the TiO_2(110) facet, the active Lewis acid−base sites are the two-coordinated bridge oxygen and five-coordinated Ti atom, highlighted in Figure S1 as O_{2c} and Ti_{5c}, respectively. We investigated all the possible sites on the pristine TiO_2 surface for thermocatalytic CH_4 adsorption and dissociation to CH_3^* and H*. However, the lowest C−H bond activation barrier (1.01 eV) was obtained on the $^{C}Ti_{5c}-{}^{H}O_{2c}$ site pair. Hence, we adopted $^{C}Ti_{5c}-{}^{H}O_{2c}$ site pairs as the active sites for the photocatalytic activation. Our DFT calculations showed that CH_4 adsorption on the (110) surface of TiO_2 is weakly exothermic with an adsorption energy of −0.30 eV, wherein CH_4 interacts mainly with d orbitals of surface Ti_{5c} atoms. Generally, CH_4 activation on oxide catalysts occurs through two potential mechanisms: polar (heterolytic) or radical (homolytic) pathways. The former mechanism involves heterolytic dissociation of CH_4 to methyl and hydrogen surface species (CH_3^-* and H^+*), whereas the latter entails the abstraction of a hydrogen radical by surface oxygen, leaving behind a methyl radical in the gas phase.[67−69] The energy barrier for the first CH_4 dissociation was found to be 1.01 eV (Figure 1a), following the heterolytic methane dissociation mechanism ($CH_4 + Ti_{5c}^{4+} + O_{2c}^{2-} \rightarrow Ti_{5c}^{4+} + CH_3^- + O_{2c}H^-$). Spin-charge distribution of the transition state ($TS1^t$) demonstrated that the O_{2c} site captures the dissociated H^+*, whereas Ti_{5c} stabilizes the CH_3^-* group (dihapto configuration). The Bader charges for the adsorbed hydrogen and methyl anion were found to be +0.56 and −0.26 |e|, respectively (Figure 1b). Additionally, the bond lengths of O_{2c}−H and C−Ti_{5c} at $TS1^t$ were 1.22 and 2.33 Å, respectively. Due to the high CH_4 activation barrier, NOCM is unlikely at room temperature, and high temperatures are required for CH_4 activation and conversion.[70]

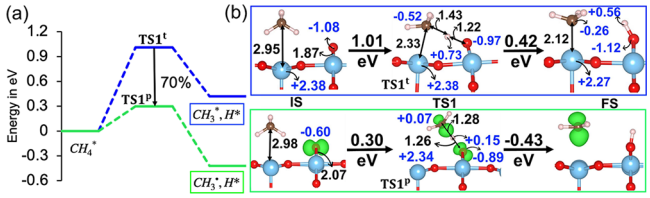

Figure 1. (a) Energy profile of the first CH_4 molecule activation by thermo- and photocatalytic pathways, depicted in blue and green, respectively. (b) Spin density distribution, bond lengths, and Bader charge population of the species involved in the elementary steps. Numerical values highlighted in blue and black indicate the Bader charge in |e| and bond length in Å, respectively. These notations are used throughout the article. The Gibbs free energy for C−H bond activation of the first CH_4 molecule is 1.42 eV at 1240 K in the case of thermocatalysis.

The photocatalytic CH_4 activation was studied by introducing a photogenerated hole into the (110) surface of TiO_2 using DFT+U with U_{2p} = 6.3 eV. The photogenerated carriers such as electrons and holes, which occur at different time scales, have the possibility of having a conduction band (CB) and valence band (VB) of the oxide, respectively. The carriers can be generated by introducing a photon with a specific wavelength, corresponding to the bandgap of the oxide. The photogenerated hole is trapped by the O_{2c} atom to generate the O_{2c}^- radical ($O_{2c}^{2-} + h^+ \rightarrow O_{2c}^-$). The green spin-density isosurface depicted in Figure 1b indicates the distribution of the hole on the slab. In the presence of the O_{2c}^- radical, CH_4 is activated homolytically to form $^{\cdot}CH_3$ radical centered on the Lewis acid site, Ti_{5c}, and the H radical bounded to O_{2c}^- ($CH_4 + O_{2c}^- \rightarrow {}^{\cdot}CH_3 + HO_{2c}^-$). Importantly, the C−H bond activation barrier drastically decreased to 0.30 eV compared to 1.01 eV of the thermocatalytic route in terms of electronic energies. Upon comparison of the TS geometries of the thermo- and photocatalytic CH_4 activation pathways, it was noticed that $TS1^t$ changes from the original dihapto configuration to a monohapto configuration ($TS1^P$). In the $TS1^P$, the CH_3−H and H−O_{2c} bond lengths were found to be 1.28 and 1.26 Å, respectively. Bader charge population and magnetic moment of $^{\cdot}CH_3$ species in $TS1^P$ were +0.07 |e| and 0.41 μ_B, respectively. Importantly, the reaction energy of the heterolytic and homolytic modes of CH_4 dissociation was 0.42 and −0.43 eV, respectively. Therefore, light-induced CH_4 activation on TiO_2, facilitated by the photogenerated hole, is kinetically and thermodynamically favored over the thermocatalytic activation of CH_4.

Zhou et al.[42] proposed that O_{2c}^-, formed from the photogenerated hole, carries fewer electrons than the O_{2c}^{2-}, hence it is easier for O_{2c}^- (open-shell configuration) to capture more electrons from the dissociated hydrogen compared to O_{2c}^{2-} (closed-shell configuration). Our analysis demonstrated that the Bader population on O_{2c}^{2-} and O_{2c}^- is −1.08 and −0.60 |e|, respectively. Therefore, the O_{2c}^- site with fewer electrons acts as a strong oxidative site with an unoccupied 2p orbital which can be associated with feasible CH_4 activation under mild reaction conditions.

The activity of the photogenerated electron−hole pairs depends on their presence on the catalyst surface. Using time-resolved absorption spectroscopy, Yamakata et al.[71,72] discovered that the most photogenerated electrons in rutile

https://doi.org/10.1021/acscatal.4c04312
ACS Catal. 2025, 15, 1195−1205

TiO_2 are deeply trapped and cannot be thermally excited to the CB or shallow states of the CB, hence exhibiting low or no reactivity toward surface reactions.[73] Additionally, it has been reported that the photogenerated electron trapped at Ti_{5c}^{4+} forms the Ti_{5c}^{3+}, which can activate methane and result in a significant reduction of the methane activation energy barrier compared to the Ti_{5c}^{4+}.[42] Notably, defect sites, such as oxygen vacancies, have been observed on the TiO_2 surface, which inherently shows an n-type behavior due to the presence of defects. Understanding the photocatalytic mechanism of oxygen-deficient TiO_2 is important and will be addressed in future studies.[74]

Activation of the Second CH_4 Molecule. Encouraged by the promising results of the photocatalytic activation of the first CH_4 molecule on the pristine TiO_2 (110) surface, we implemented a similar approach to activate a second CH_4 molecule with another photogenerated hole. Our calculations found that creating a second hole adjacent to the first hole, with the U_{2p} = 6.3 eV, is impossible due to the repulsion between the two hole-polarons. A similar observation was reported by Reticcioli et al.[41] for the formation of two-electron polarons on adjacent Ti atoms within 2.97 Å on the rutile TiO_2 (110) surface. Therefore, for the second CH_4 activation, we adopted U_{2p} = 8.5 eV to create the second hole, where the distance between the two hole-polarons is ∼7.2 Å. The PDOS and hole polaron formation energies are presented in Figure S1 and Table S2.

Initially, a second hole was created by removing another electron from the system or attaching another F atom on the bottom of the slab, followed by the adsorption of a second CH_4 molecule on another Ti_{5c} site that is adjacent to the first $^{\cdot}CH_3$ radical. Figure 2 shows the energetics of the second CH_4

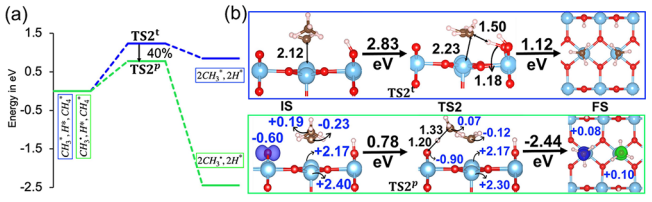

Figure 2. (a) Energy profile of the second CH_4 molecule activation by thermo- and photocatalytic pathways, where holes are formed by removing electrons from the system. Blue and green lines depict the thermocatalytic and photocatalytic pathways, respectively. (b) Spin density distribution, bond lengths, and Bader charge population of the species involved in the elementary steps. The Gibbs free energy for C−H bond activation of second CH_4 molecule is 1.73 eV at 1240 K in the case of thermocatalysis.

activation via thermo- and photocatalytic routes. The spin density and Bader charge on O_{2c} confirmed the generation of the photogenerated hole with a −0.3 |e| charge gain (−0.60 vs −0.90 |e|). Similar to the first CH_4 activation, the barrier for photocatalytic activation of the second CH_4 molecule is significantly lower by 40% compared to that of the thermocatalysis route. We note, however, that the photocatalytic activation of the second CH_4 molecule is more energy-demanding (0.30 eV vs 0.78 eV) than that of the first CH_4 molecule (Figure 2a). This is due to the steric hindrance between the second adsorbed CH_4 and the previously dissociated one, necessitating a substantially higher energy barrier to activate the second CH_4 molecule. It was found that the first $^{\cdot}CH_3$ becomes the surface-mediated species with a Bader population of −0.23 |e| due to the above-mentioned steric hindrance effect, as depicted in Figure 2b. Additionally, $TS1^P$ geometry confirmed homolytic dissociation of the second CH_4 molecule to the $^{\cdot}CH_3$ radical, with a Bader charge of +0.07 |e|. The magnetic moment on the two $^{\cdot}CH_3$ radicals was the same (0.41 μ_B) in opposite directions. Together, the dissociation of two CH_4 molecules resulted in two $^{\cdot}CH_3$ radicals, key intermediates for mild temperature NOCM to C_2 hydrocarbons.[7,13,24]

Nonoxidative Coupling of CH_4 to Ethane. So far, our calculations demonstrate the superior performance of the photogenerated holes on TiO_2 for CH_4 activation through the formation of gas-phase $^{\cdot}CH_3$ radicals. The generated $^{\cdot}CH_3$ radicals can further couple to form ethane. Figure 3 depicts the

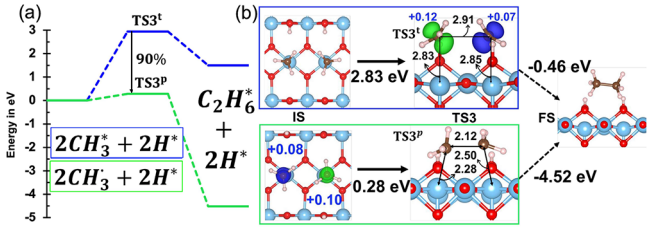

Figure 3. (a) Energy profile of the C−C coupling reaction by thermo- and photocatalytic pathways, where holes are formed by removing electrons from the system. Blue and green line depict the thermocatalytic and photocatalytic pathways, respectively. (b) Spin density distribution, bond lengths, and Bader charge population of the species involved in the elementary steps. The Gibbs free energy for C−C coupling reaction is 2.93 eV at 1240 K in case of thermocatalysis.

energetics of the thermo- and photocatalytic NOCM to ethane in addition to the spin density distribution of the initial and transition states. Thermocatalytic ethane formation through the coupling of two surface CH_3^-* species was kinetically hindered with a high barrier of 2.83 eV. Additionally, ethane desorption was found to be endothermic, with a desorption reaction energy of 0.44 eV. Conversely, the energy barrier for photocatalytic C−C coupling of two $^{\cdot}CH_3$ radicals was 0.28 eV, which is 90% lower than that of the theromocatalytic mode. The Bader charge on $^{\cdot}CH_3$ radicals at the TS was +0.12 and +0.07 |e|, confirming their radical nature. The dramatic decrease in the C−C coupling energy barrier, from 2.83 to 0.28 eV, confirms that the photogenerated holes play a vital role in overcoming the uphill kinetic barrier in thermocatalytic NOCM. Notably, the photocatalytic C−C coupling reaction was found to be highly exothermic (−0.46 vs −4.52 eV) compared to the thermocatalytic mode. It should be noted that the distinct lifetimes of $^{\cdot}CH_3$ radicals and photogenerated holes under reaction conditions may reduce the probability of sequential CH_4 activation events and limit the formation of C_2 products.[75,76] Depending on the source of formation, the lifetime of $^{\cdot}CH_3$ radicals can be varied from milliseconds to seconds, whereas surface-trapped holes are trapped in VB of rutile in less than 80 μs and the reaction with CH_4 can occur in the ps−ns range.[77−79]

Molecular Hydrogen Formation. Figure 4 shows the H_2 formation pathways on positively charged TiO_2(110). Generally, molecular H_2 can be formed by the combination of two dissociated hydrogens bound to O_{2c} and O_{3c} sites.[64] However, hydrogen diffusion steps are necessary for the formation of molecular H_2 because the dissociated hydrogens

https://doi.org/10.1021/acscatal.4c04312
ACS Catal. 2025, 15, 1195−1205

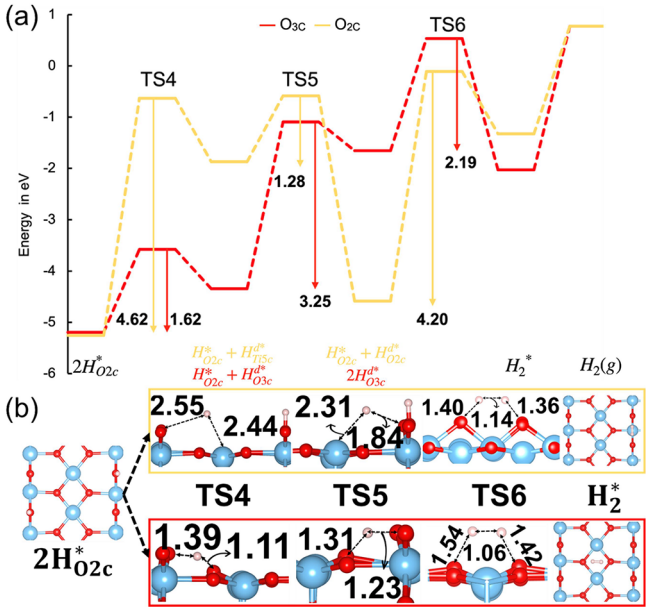

Figure 4. Energy profile of hydrogen diffusion and molecular H_2 formation on the positively charged (110) TiO_2 system, where d indicates a diffused atom. H_2 formation mechanisms from O_{2c} and O_{3c} are colored orange and red, respectively.

are far from each other, as depicted in Figures 1 and 2. Regarding the hydrogen bound to O_{2c}, the diffusion barrier to the Ti_{5c} site was found to be 4.62 eV. The hydrogen further diffuses from Ti_{5c} to the O_{2c} site that is adjacent to the second dissociated hydrogen, with a barrier of 1.28 eV. Finally, H_2 formation occurs via recombination of the two hydrogens bound to O_{2c} sites through a high energy barrier of 4.20 eV. Additionally, we investigated another route for H_2 formation which includes diffusion of one hydrogen from O_{2c} to a neighboring O_{3c}. This diffusion event occurs through a barrier of 1.62 eV. Then, the second dissociated hydrogen diffuses from O_{2c} to a nearby O_{3c} site, with a barrier of 3.25 eV. Finally, H_2 formation from these dissociated hydrogens involves a high energy barrier of 2.19 eV. We noted that hydrogen formation on TiO_2 is the most energetically demanding step in the NOCM reaction network. Yuliti et al. also suggested that after the formation of ethane by NOCM, the catalyst surface is poisoned, and hydrogen species were found to reduce the surface under UV radiation.[14]

Insight into the Photocatalytic NOCM to Ethane and H_2 Molecules. As noted, the photocatalytic performance of TiO_2 evaluated by DFT calculations does not consider experimental reaction conditions, including temperature, partial pressure of gas phase species, and the global effect of elementary reactions, such as forward and reverse reaction rates. Based on our DFT results, we performed kMC simulations to evaluate the kinetics of the photocatalytic NOCM to ethane and H_2 molecules on rutile TiO_2 under experimental reaction conditions of T = 315.15 K and $p(CH_4)$ = 1.0 bar. The convergence of the kMC simulations with respect to the size of the kMC lattice was tested by performing the same kMC simulations using a 2D (40 × 40) kMC supercell (a total of 1600 sites, four times the size of the 2D 20 × 20 supercell). The calculated kinetic parameters, including surface coverage, were not affected by the size of the lattice or by the random seed, as shown in Figure S7. Based on the convergence test, we chose the 20 × 20 kMC supercell for our investigation. Adsorbate−adsorbate interactions can substantially affect the adsorption energy and activation energy barriers. The estimates of the adsorbate−adsorbate interactions have been tested by comparing the binding energy of dissociated CH_3^-* and H^+* surface species and the sum of binding energies of the isolated surface with CH_3^-* and another isolated surface with H^+* on different active site pairs of TiO_2 surface, as depicted in Table S4. For the dissociated CH_3^-* and H^+* species, the calculated DFT binding energies were found to be 1.33−3.96 eV higher than the sum of isolated surface species, which reveals a significant repulsion between dissociated CH_3^-* and H^+* species on the (110) TiO_2 surface. Due to substantial repulsive forces between surface species in the DFT energetics forming the basis of the kMC simulations, additional lateral interaction models were not incorporated in the simulations.

The kMC simulations included five elementary steps: light irradiation, CH_4 photoactivation, C−C coupling to ethane, hydrogen diffusion, and H_2 formation events. CH_4 adsorption and desorption events were not included in the kMC simulations. Instead, we assumed an initial preadsorbed CH_4 coverage based on experimental saturation data to focus on surface reactions driven by photoexcitation. In the kMC simulations, TiO_2 is first illuminated by UV light, leading to

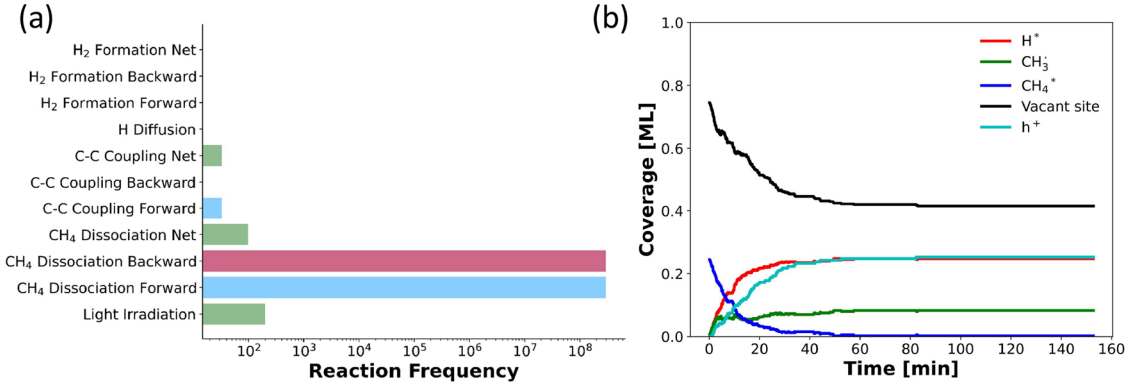

Figure 5. (a) Main elementary processes and their frequencies for photocatalytic NOCM to ethane at 315.15 K for a 2D (20 × 20) kMC supercell. The number of each reaction frequency is plotted on the log10 scale. (b) Fractional coverage of the different species as a function of time. T = 315.15 K, and P = 1 bar.

https://doi.org/10.1021/acscatal.4c04312
ACS Catal. 2025, 15, 1195−1205

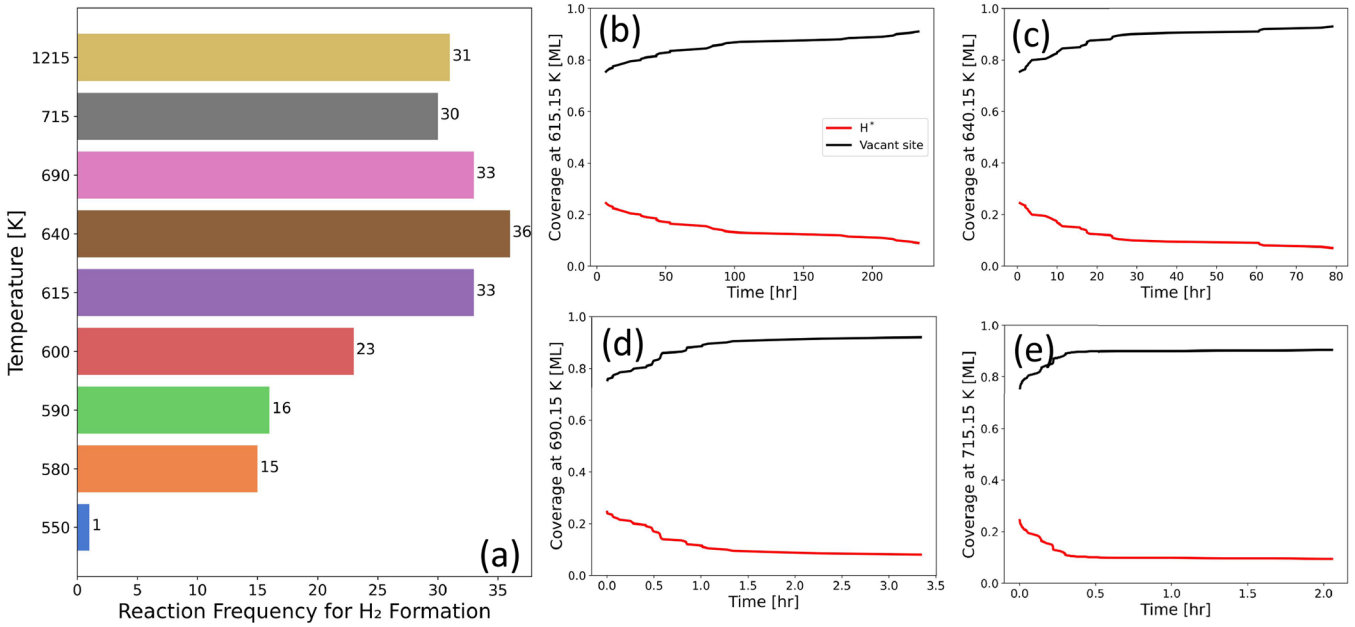

Figure 6. (a) Net H_2 formation event frequency at different temperatures. Fractional coverages of H* species as a function of time at (b) 615.15, (c) 640.15, (d) 690.15, and (e) 715.15 K.

the formation of electron−hole pairs where the photogenerated hole is trapped by the surface O_{2c}^{2-} to generate $O_{2c}^{\cdot-}$ (hole polaron). The photoirradiation reaction was assumed to occur instantly upon exposure of TiO_2 to a UV light beam. Hence, the irradiation reaction rate was governed mainly by the intensity of the UV light beam, which was assumed to be constant during the reaction. Additionally, the initial coverage of CH_4 was set to 0.25 ML, as calculated from the experimental saturation of CH_4 on TiO_2 P25 catalyst (containing a mixture of both anatase and rutile phases of TiO_2) under light in the absence of O_2 at 315.15 K.[60] It is assumed that upon light excitation of the catalyst, CH_4 molecules dissociate immediately to form $^{\cdot}CH_3$ radicals and H* species. Figure 5a highlights the frequency of the events of each elementary reaction. As noted earlier, the photogenerated holes in the valence band are essential for the activation of CH_4. Hence, once the hole polaron is formed, CH_4 is photoactivated to the $^{\cdot}CH_3$ intermediate and H* adsorbed on the $O_{2c}^{\cdot-}$. We note that CH_4 photoactivation occurs significantly faster than the remaining processes under the reaction conditions, with a net forward rate. After the formation of $^{\cdot}CH_3$ radicals, ethane was formed via the coupling of two $^{\cdot}CH_3$ radicals, where the amount of formed ethane depends on the frequency of CH_4 dissociation to $^{\cdot}CH_3$ radicals. Given a net of 99 CH_4 dissociation events, 33 ethane molecules were formed and desorbed to the gas phase, with a net TOF of 9×10^{-6} s^{-1}. Under the reaction conditions of 313.15 K, the kMC simulation did not perform any hydrogen diffusion or H_2 formation events. This result is obvious based on the DFT energetics where hydrogen diffusion and H_2 formation are associated with significantly higher barriers than CH_4 activation and C−C coupling elementary reaction steps (as shown in Figures 3 and 4).

To determine the reaction time to reach a steady state, the fractional coverages were simulated as a function of time, as demonstrated in Figure 5b. The reaction reached a steady state after 60 min when all CH_4 species were photoactivated to $^{\cdot}CH_3$ radicals. Importantly, surface hydrogen was found to be the most abundant surface species with 0.25 ML fractional coverage at steady state, gradually blocking the O_{2c} active sites. This is due to the high energy barriers for H_2 formation of 4.2 eV. Based on the above analysis, photoactivated TiO_2 has a high event frequency of ethane formation; however, the catalyst is poisoned with hydrogen species under room-temperature reaction conditions.

It is noted that traditional static catalytic sites attempt to balance multiple elementary reaction steps within the surface reaction network. However, an optimal site for product desorption may not necessarily be ideal for reactant adsorption and the following surface reactions. On the other side, dynamic catalysis, which involves modulating adsorbate binding energies, offers a transformative approach to overcoming these limitations.[80] For instance, Christopher and co-workers[81] regulated the binding energy of surface intermediates on Pt nanoparticle catalysts using pulsed illumination, leading to an improved activity of H_2 production compared to static illumination. Additionally, Baldi and Askes[82] revealed that pulsed photothermal catalysis can control surface coverages, increase robustness against catalyst poisons, and achieve higher turnover per site compared to steady-state heating methods. Besides, Sordello et al.[83] showcased that controlled periodic illumination (i.e., alternating between light and dark periods) improves the efficiency of the hydrogen evolution reaction over metals photodeposited on TiO_2 nanoparticles compared to continuous illumination. In the context of photocatalytic NOCM on TiO_2, the photogenerated holes facilitated CH_4 dissociation and C−C coupling to ethane, however, H_2 formation was kinetically hindered, necessitating a dynamic approach to regenerate catalytic activity. Through synergetic catalytic processes leveraging both thermal and photo energies, the dynamic active sites of TiO_2 can adapt over the catalytic cycle, providing an optimal energetic environment for each elementary step in the NOCM reaction network.[81]

Temporarily rising the simulation temperature can facilitate H_2 formation and regenerate the O_{2c} active sites. For this scenario, we used thermocatalytic H_2 formation energetics of a

https://doi.org/10.1021/acscatal.4c04312
ACS Catal. 2025, 15, 1195−1205

neutral TiO_2(110) surface (Figure S8) in the kMC simulations. Accordingly, UV-light irradiation was turned off in the kMC simulations after all CH_4 species were photoactivated and converted to ethane (and the surface was dominated by H* species with a steady state surface coverage of 0.25 ML), and then the reaction temperature was raised gradually from 315.15 to 1215.15 K (typical temperature of thermal NOCM reaction). As shown in Figure 6, hydrogen species started desorbing as molecular hydrogen at 615.15 K, with a net H_2 formation reaction frequency of 33 events (Figure 6a) and steady-state surface hydrogen coverage of 0.085 ML (Figure 6b). However, the rate of hydrogen production at 615.15 was substantially slow. Raising the temperature to 690.15 K resulted in significantly faster hydrogen production, with complete surface regeneration within less than 1 h, as illustrated in Figure 6d. The gradual increase of the reaction temperature above 690.15 K had a minimal influence on the hydrogen coverage and the net H_2 formation reaction frequency. Therefore, it is deemed unnecessary since the catalytic surface was regenerated at 690.15 K, a temperature that is significantly lower than the typical thermocatalytic NOCM reaction temperature.[13]

In summary, kMC simulations reveal that NOCM to ethane and hydrogen on rutile TiO_2 is feasible through a combined photo- and thermocatalysis process. However, it is important to highlight that there is a significant disparity in the time scales between thermal and photoinduced processes, which can present technical challenges in practical applications. For instance, photocatalytic processes generally occur on short time scales, with photon absorption occurring on the order of femtoseconds (10^{-15} seconds). In contrast, thermochemical reactions typically unfold over longer time scales, often ranging from minutes to hours, depending on the specific thermal treatment conditions applied. This difference in time scales can complicate the integration of thermal and photocatalytic processes, as it may be challenging to synchronize the two mechanisms effectively. To achieve the effectiveness of photothermal approaches in real-world applications, it is crucial to develop strategies that account for the sequential nature of these processes. Optimizing the timing and conditions for thermal treatments in conjunction with photocatalytic reactions could enhance the overall system performance and efficiency.[84−87]

CONCLUSIONS

In this contribution, we combined periodic DFT and kMC simulations to provide a comprehensive understanding of the NOCM reaction on pristine TiO_2 through synergistic photo- and thermo-catalytic production of ethane and H_2, respectively. DFT calculations illustrated the importance of the photogenerated holes for facile CH_4 dissociation and C−C coupling to ethane compared to the thermocatalytic route. Further, kMC simulations revealed that the formation of ethane product via the recombination of $^{\cdot}CH_3$ radicals can occur at mild temperatures of 315.15 K. However, the active sites are poisoned by adsorbed hydrogen. To facilitate H_2 formation and catalyst regeneration after photocatalytic ethane formation, the reaction temperature was raised to 690.15 K, which is significantly lower than the typical NOCM temperatures. Thus, we propose that NOCM to ethane and hydrogen on pristine TiO_2 can occur with dynamic catalysis, where photo- and thermocatalytic modes are combined. In addition to providing mechanistic insights into the photocatalytic NOCM on TiO_2, this work demonstrates novel routes for dynamic catalysis simulations through multiscale modeling, opening new paths for discovering highly selective and active catalysts.

ASSOCIATED CONTENT

Supporting Information

The Supporting Information is available free of charge at https://pubs.acs.org/doi/10.1021/acscatal.4c04312.

Detailed photocatalytic energetic pathways of NOCM and computational details of DFT+U calculations and kMC simulations (PDF)

AUTHOR INFORMATION

Corresponding Author

Giannis Mpourmpakis − *Department of Chemical and Petroleum Engineering, University of Pittsburgh, Pittsburgh, Pennsylvania 15261, United States;* Present Address: School of Chemical Engineering, National Technical University of Athens (NTUA), Athens, GR-15780, Greece; orcid.org/0000-0002-3063-0607; Email: gmpourmp@pitt.edu

Authors

Juganta K. Roy − *Department of Chemical and Petroleum Engineering, University of Pittsburgh, Pittsburgh, Pennsylvania 15261, United States; Department of Chemistry and Physics, West Texas A&M University, Canyon, Texas 79106, United States;* orcid.org/0000-0002-3646-5593

Mona Abdelgaid − *Department of Chemical and Petroleum Engineering, University of Pittsburgh, Pittsburgh, Pennsylvania 15261, United States;* orcid.org/0000-0003-0973-3262

Henrik Grönbeck − *Department of Physics and Competence Centre for Catalysis, Chalmers University of Technology, 412 96 Göteborg, Sweden*

Complete contact information is available at: https://pubs.acs.org/10.1021/acscatal.4c04312

Notes

The authors declare no competing financial interest.

ACKNOWLEDGMENTS

This work is supported by the American Chemical Society Petroleum Research Fund (ACS-PRF: 62418-ND5). G.M. acknowledges sabbatical support from Chalmers University of Technology, Areas of Advance: Materials Science, and the Wenner Gren Foundation. High-performance computational support was provided by the Center for Research Computing (CRC) at the University of Pittsburgh, and the Advanced Cyberinfrastructure Coordination Ecosystem: Services & Support (ACCESS) program supported by the NSF (ACI-1053575). Most of the computations were performed in Expanse at San Diego Supercomputer Center (SDSC) through allocation ACI-1053575 from the ACCESS program, which is supported by National Science Foundation grants #2138259, #2138286, #2138307, #2137603, and #2138296. Also, this research was supported in part by the University of Pittsburgh Center for Research Computing, RRID:SCR_022735, through the resources provided. Specifically, this work used the H2P

cluster, which is supported by NSF award number OAC-2117681.

REFERENCES

(1) Schwach, P.; Pan, X.; Bao, X. Direct Conversion of Methane to Value-Added Chemicals over Heterogeneous Catalysts: Challenges and Prospects. *Chem. Rev.* **2017**, *117* (13), 8497−8520.
(2) Kerr, R. A. Natural Gas From Shale Bursts Onto the Scene. *Science (1979)* **2010**, *328* (5986), 1624−1626.
(3) Tang, P.; Zhu, Q.; Wu, Z.; Ma, D. Methane Activation: The Past and Future. *Energy Environ. Sci.* **2014**, *7* (8), 2580−2591.
(4) Linsebigler, A. L.; Lu, G.; Yates, J. T. Photocatalysis on TiO_2 Surfaces: Principles, Mechanisms, and Selected Results. *Chem. Rev.* **1995**, *95* (3), 735−758.
(5) Horn, R.; Schlögl, R. Methane Activation by Heterogeneous Catalysis. *Catal. Lett.* **2015**, *145* (1), 23−39.
(6) Olivos-Suarez, A. I.; Szécsényi, À.; Hensen, E. J. M.; Ruiz-Martinez, J.; Pidko, E. A.; Gascon, J. Strategies for the Direct Catalytic Valorization of Methane Using Heterogeneous Catalysis: Challenges and Opportunities. *ACS Catal.* **2016**, *6* (5), 2965−2981.
(7) Yuliati, L.; Yoshida, H. Photocatalytic Conversion of Methane. *Chem. Soc. Rev.* **2008**, *37* (8), 1592.
(8) Kwon, Y.; Kim, T. Y.; Kwon, G.; Yi, J.; Lee, H. Selective Activation of Methane on Single-Atom Catalyst of Rhodium Dispersed on Zirconia for Direct Conversion. *J. Am. Chem. Soc.* **2017**, *139* (48), 17694−17699.
(9) Latimer, A. A.; Kulkarni, A. R.; Aljama, H.; Montoya, J. H.; Yoo, J. S.; Tsai, C.; Abild-Pedersen, F.; Studt, F.; Nørskov, J. K. Understanding Trends in C-H Bond Activation in Heterogeneous Catalysis. *Nat. Mater.* **2017**, *16* (2), 225−229.
(10) Ito, T.; Lunsford, J. H. Synthesis of Ethylene and Ethane by Partial Oxidation of Methane over Lithium-Doped Magnesium Oxide. *Nature* **1985**, *314* (6013), 721−722.
(11) Wang, P.; Zhao, G.; Wang, Y.; Lu, Y. $MnTiO_3$ -Driven Low-Temperature Oxidative Coupling of Methane over TiO_2 -Doped Mn_2O_3-Na_2WO_4/SiO_2 Catalyst. *Sci. Adv.* **2017**, *3* (6), No. e1603180.
(12) Wang, G.; Mu, X.; Li, J.; Zhan, Q.; Qian, Y.; Mu, X.; Li, L. Light-Induced Nonoxidative Coupling of Methane Using Stable Solid Solutions. *Angewandte Chemie - International Edition* **2021**, *60* (38), 20760−20764.
(13) Guo, X.; Fang, G.; Li, G.; Ma, H.; Fan, H.; Yu, L.; Ma, C.; Wu, X.; Deng, D.; Wei, M.; Tan, D.; Si, R.; Zhang, S.; Li, J.; Sun, L.; Tang, Z.; Pan, X.; Bao, X. Direct, Nonoxidative Conversion of Methane to Ethylene, Aromatics, and Hydrogen. *Science (1979)* **2014**, *344* (6184), 616−619.
(14) Yuliati, L.; Ltoh, H.; Yoshida, H. Preparation of Isolated Highly Dispersed Titanium Oxides on Silica by Sol-Gel Method for Photocatalytic Non-Oxidative Direct Methane Coupling. *Stud. Surf. Sci. Catal.* **2006**, *162*, 961−968.
(15) Sattler, J. J. H. B.; Ruiz-Martinez, J.; Santillan-Jimenez, E.; Weckhuysen, B. M. Catalytic Dehydrogenation of Light Alkanes on Metals and Metal Oxides. *Chem. Rev.* **2014**, *114* (20), 10613−10653.
(16) Lunsford, J. H. The Catalytic Oxidative Coupling of Methane. *Angewandte Chemie International Edition in English* **1995**, *34* (9), 970−980.
(17) Xiao, Y.; Varma, A. Highly Selective Nonoxidative Coupling of Methane over Pt-Bi Bimetallic Catalysts. *ACS Catal.* **2018**, *8* (4), 2735−2740.
(18) Xie, S.; Ma, W.; Wu, X.; Zhang, H.; Zhang, Q.; Wang, Y.; Wang, Y. Photocatalytic and Electrocatalytic Transformations of C1Molecules Involving C−C Coupling. *Energy Environ. Sci.* **2021**, *14* (1), 37−89.
(19) Hu, D.; Ordomsky, V. V.; Khodakov, A. Y. Major Routes in the Photocatalytic Methane Conversion into Chemicals and Fuels under Mild Conditions. *Appl. Catal., B* **2021**, *286*, No. 119913.
(20) Chen, Z.; Wu, S.; Ma, J.; Mine, S.; Toyao, T.; Matsuoka, M.; Wang, L.; Zhang, J. Non-Oxidative Coupling of Methane: N-Type Doping of Niobium Single Atoms in TiO2−SiO2 Induces Electron Localization. *Angewandte Chemie - International Edition* **2021**, *60* (21), 11901−11909.
(21) Lang, J.; Ma, Y.; Wu, X.; Jiang, Y.; Hu, Y. H. Highly Efficient Light-Driven Methane Coupling under Ambient Conditions Based on an Integrated Design of a Photocatalytic System. *Green Chem.* **2020**, *22* (14), 4669−4675.
(22) Sato, H.; Ishikawa, A.; Saito, H.; Higashi, T.; Takeyasu, K.; Sugimoto, T. Critical Impacts of Interfacial Water on C−H Activation in Photocatalytic Methane Conversion. *Commun. Chem.* **2023**, *6* (1), 8.
(23) Yu, X.; Zholobenko, V. L.; Moldovan, S.; Hu, D.; Wu, D.; Ordomsky, V. V.; Khodakov, A. Y. Stoichiometric Methane Conversion to Ethane Using Photochemical Looping at Ambient Temperature. *Nat. Energy* **2020**, *5* (7), 511−519.
(24) Zhang, W.; Fu, C.; Low, J.; Duan, D.; Ma, J.; Jiang, W.; Chen, Y.; Liu, H.; Qi, Z.; Long, R.; Yao, Y.; Li, X.; Zhang, H.; Liu, Z.; Yang, J.; Zou, Z.; Xiong, Y. High-Performance Photocatalytic Nonoxidative Conversion of Methane to Ethane and Hydrogen by Heteroatoms-Engineered TiO_2. *Nature Communications 2022 13:1* **2022**, *13* (1), 1−9.
(25) Meng, X.; Cui, X.; Rajan, N. P.; Yu, L.; Deng, D.; Bao, X. Direct Methane Conversion under Mild Condition by Thermo-, Electro-, or Photocatalysis. *Chem.* **2019**, *5* (9), 2296−2325.
(26) Zhao, Y.; Gao, W.; Li, S.; Williams, G. R.; Mahadi, A. H.; Ma, D. Solar- versus Thermal-Driven Catalysis for Energy Conversion. *Joule* **2019**, *3* (4), 920−937.
(27) Wei, J.; Yang, J.; Wen, Z.; Dai, J.; Li, Y.; Yao, B. Efficient Photocatalytic Oxidation of Methane over β-Ga_2O_3/Activated Carbon Composites. *RSC Adv.* **2017**, *7* (60), 37508−37521.
(28) Chen, X.; Li, Y.; Pan, X.; Cortie, D.; Huang, X.; Yi, Z. Photocatalytic Oxidation of Methane over Silver Decorated Zinc Oxide Nanocatalysts. *Nat. Commun.* **2016**, *7*, 12273.
(29) Pan, X.; Chen, X.; Yi, Z. Photocatalytic Oxidation of Methane over $SrCO_3$ Decorated $SrTiO_3$ Nanocatalysts via a Synergistic Effect. *Phys. Chem. Chem. Phys.* **2016**, *18* (46), 31400−31409.
(30) Schwach, P.; Pan, X.; Bao, X. Direct Conversion of Methane to Value-Added Chemicals over Heterogeneous Catalysts: Challenges and Prospects. *Chem. Rev.* **2017**, *117* (13), 8497−8520.
(31) Kresse, G.; Joubert, D. From Ultrasoft Pseudopotentials to the Projector Augmented-Wave Method. *Phys. Rev. B* **1999**, *59* (3), 1758−1775.
(32) Kresse, G.; Furthmüller, J. Efficiency of Ab-Initio Total Energy Calculations for Metals and Semiconductors Using a Plane-Wave Basis Set. *Comput. Mater. Sci.* **1996**, *6* (1), 15−50.
(33) Kresse, G.; Hafner, J. Ab Initio Molecular-Dynamics Simulation of the Liquid-Metal−Amorphous-Semiconductor Transition in Germanium. *Phys. Rev. B* **1994**, *49* (20), 14251−14269.
(34) Kresse, G.; Furthmüller, J. Efficient Iterative Schemes for Ab Initio Total-Energy Calculations Using a Plane-Wave Basis Set. *Phys. Rev. B* **1996**, *54* (16), 11169−11186.
(35) Perdew, J. P.; Burke, K.; Ernzerhof, M. Generalized Gradient Approximation Made Simple. *Phys. Rev. Lett.* **1996**, *77* (18), 3865−3868.
(36) Grimme, S.; Antony, J.; Ehrlich, S.; Krieg, H. A Consistent and Accurate Ab Initio Parametrization of Density Functional Dispersion Correction (DFT-D) for the 94 Elements H-Pu. *J. Chem. Phys.* **2010**, *132* (15), 154104.
(37) Grimme, S.; Ehrlich, S.; Goerigk, L. Effect of the Damping Function in Dispersion Corrected Density Functional Theory. *J. Comput. Chem.* **2011**, *32* (7), 1456−1465.
(38) Anisimov, V. I.; Zaanen, J.; Andersen, O. K. Band Theory and Mott Insulators: Hubbard *U* Instead of Stoner *I*. *Phys. Rev. B* **1991**, *44* (3), 943−954.
(39) Heyd, J.; Scuseria, G. E. Efficient Hybrid Density Functional Calculations in Solids: Assessment of the Heyd−Scuseria−Ernzerhof Screened Coulomb Hybrid Functional. *J. Chem. Phys.* **2004**, *121* (3), 1187−1192.
(40) Dudarev, S. L.; Botton, G. A.; Savrasov, S. Y.; Humphreys, C. J.; Sutton, A. P. Electron-Energy-Loss Spectra and the Structural Stability

https://doi.org/10.1021/acscatal.4c04312
ACS Catal. 2025, 15, 1195−1205

of Nickel Oxide: An LSDA+U Study. *Phys. Rev. B* **1998**, *57* (3), 1505−1509.
(41) Reticcioli, M.; Setvin, M.; Schmid, M.; Diebold, U.; Franchini, C. Formation and Dynamics of Small Polarons on the Rutile TiO_2(110) Surface. *Phys. Rev. B* **2018**, *98*, No. 045306.
(42) Zhou, M.; Wang, H. Optimally Selecting Photo- and Electrocatalysis to Facilitate CH_4 Activation on TiO_2(110) Surface: Localized Photoexcitation versus Global Electric-Field Polarization. *JACS Au* **2022**, *2* (1), 188−196.
(43) German, E.; Faccio, R.; Mombrú, A. W. A DFT + *U* Study on Structural, Electronic, Vibrational and Thermodynamic Properties of TiO $_2$ Polymorphs and Hydrogen Titanate: Tuning the Hubbard '*U* -Term.'. *J. Phys. Commun.* **2017**, *1* (5), No. 055006.
(44) Heyd, J.; Scuseria, G. E.; Ernzerhof, M. Hybrid Functionals Based on a Screened Coulomb Potential. *J. Chem. Phys.* **2003**, *118* (18), 8207−8215.
(45) Henkelman, G.; Jónsson, H. Improved Tangent Estimate in the Nudged Elastic Band Method for Finding Minimum Energy Paths and Saddle Points. *J. Chem. Phys.* **2000**, *113* (22), 9978−9985.
(46) Henkelman, G.; Jónsson, H. A Dimer Method for Finding Saddle Points on High Dimensional Potential Surfaces Using Only First Derivatives. *J. Chem. Phys.* **1999**, *111* (15), 7010−7022.
(47) Abdelgaid, M.; Dean, J.; Mpourmpakis, G. Improving Alkane Dehydrogenation Activity on γ-Al_2O_3 through Ga Doping. *Catal. Sci. Technol.* **2020**, *10* (21), 7194−7202.
(48) Zhang, J.; Peng, C.; Wang, H.; Hu, P. Identifying the Role of Photogenerated Holes in Photocatalytic Methanol Dissociation on Rutile TiO_2(110). *ACS Catal.* **2017**, *7* (4), 2374−2380.
(49) Ji, Y.; Wang, B.; Luo, Y. GGA+U Study on the Mechanism of Photodecomposition of Water Adsorbed on Rutile TiO2(110) Surface: Free vs Trapped Hole. *J. Phys. Chem. C* **2014**, *118* (2), 1027−1034.
(50) Li, F.; Chen, X.; Lai, Y.; Wang, T.; Yang, X.; Guo, Q. Low-Temperature C−H Bond Activation via Photocatalysis: Highly Efficient Ethylbenzene Dehydrogenation into Styrene on Rutile TiO_2(110). *J. Phys. Chem. Lett.* **2022**, *13* (39), 9186−9194.
(51) Liu, Z.; Balbuena, P. B.; Mukherjee, P. P. Hole Polaron Diffusion in the Final Discharge Product of Lithium−Sulfur Batteries. *J. Phys. Chem. C* **2017**, *121* (32), 17169−17175.
(52) Duc Pham, T.; Aaron Deskins, N. Efficient Method for Modeling Polarons Using Electronic Structure Methods. *J. Chem. Theory Comput* **2020**, *16* (8), 5264−5278.
(53) Kokott, S.; Levchenko, S. V.; Rinke, P.; Scheffler, M. First-Principles Supercell Calculations of Small Polarons with Proper Account for Long-Range Polarization Effects. *New J. Phys.* **2018**, *20*, No. 033023.
(54) Abdelgaid, M.; Miu, E. V; Kwon, H.; Kauppinen, M. M.; Grönbeck, H.; Mpourmpakis, G. Multiscale Modeling Reveals Aluminum Nitride as an Efficient Propane Dehydrogenation Catalyst. *Catal. Sci. Technol.* **2023**, *13*, 3527−3536.
(55) Cramer, C. J. *Essentials of Computational Chemistry: Theories and Models*, 2nd ed.; John Wiley & Sons, Ltd: Chichester, West Sussex, 2004.
(56) Jørgensen, M.; Grönbeck, H. MonteCoffee: A Programmable Kinetic Monte Carlo Framework. *J. Chem. Phys.* **2018**, *149* (11), 114101.
(57) Jansen, A. P. J. *An Introduction to Kinetic Monte Carlo Simulations of Surface Reactions*; Springer Berlin Heidelberg: Berlin, Heidelberg, 2012; vol *856*.
(58) Shams Ghamsari, Z.; Bashiri, H. Hydrogen Production through Photoreforming of Methanol by Cu(s)/TiO_2 Nanocatalyst: Optimization and Simulation. *Surfaces and Interfaces* **2020**, *21*, No. 100709.
(59) Moradmand Jalali, H. Kinetic Investigation of Photo-Catalytic Activity of TiO_2 /Metal Nanocomposite in Phenol Photo-Degradation Using Monte Carlo Simulation. *RSC Adv.* **2015**, *5* (45), 36108−36116.
(60) Thampi, K. R.; Kiwi, J.; Grätzel, M. Room Temperature Photo-Activation of Methane on TiO_2 Supported Molybdena. *Catal. Lett.* **1988**, *1* (5), 109−116.
(61) Chu, W.; Saidi, W. A.; Zheng, Q.; Xie, Y.; Lan, Z.; Prezhdo, O. V.; Petek, H.; Zhao, J. Ultrafast Dynamics of Photongenerated Holes at a CH_3OH/TiO_2 Rutile Interface. *J. Am. Chem. Soc.* **2016**, *138* (41), 13740−13749.
(62) Carp, O.; Huisman, C. L.; Reller, A. Photoinduced Reactivity of Titanium Dioxide. *Prog. Solid State Chem.* **2004**, *32* (1−2), 33−177.
(63) Kavan, L.; Grätzel, M.; Gilbert, S. E.; Klemenz, C.; Scheel, H. J. Electrochemical and Photoelectrochemical Investigation of Single-Crystal Anatase. *J. Am. Chem. Soc.* **1996**, *118* (28), 6716−6723.
(64) Abdelgaid, M.; Mpourmpakis, G. Structure−Activity Relationships in Lewis Acid−Base Heterogeneous Catalysis. *ACS Catal.* **2022**, *12*, 4268−4289.
(65) Tsuji, Y.; Yoshizawa, K. Adsorption and Activation of Methane on the (110) Surface of Rutile-Type Metal Dioxides. *J. Phys. Chem. C* **2018**, *122*, 15359−15381.
(66) Cholewinski, M. C.; Dixit, M.; Mpourmpakis, G. Computational Study of Methane Activation on γ-Al_2O_3. *ACS Omega* **2018**, *3* (12), 18242−18250.
(67) Weaver, J. F.; Hakanoglu, C.; Antony, A.; Asthagiri, A. Alkane Activation on Crystalline Metal Oxide Surfaces. *Chem. Soc. Rev.* **2014**, *43* (22), 7536−7547.
(68) Senanayake, S. D.; Rodriguez, J. A.; Weaver, J. F. Low Temperature Activation of Methane on Metal-Oxides and Complex Interfaces: Insights from Surface Science. *Acc. Chem. Res.* **2020**, *53* (8), 1488−1497.
(69) Cholewinski, M. C.; Dixit, M.; Mpourmpakis, G. Computational Study of Methane Activation on γ-Al2O3. *ACS Omega* **2018**, *3* (12), 18242−18250.
(70) Van den Bossche, M.; Grönbeck, H. Methane Oxidation over PdO(101) Revealed by First-Principles Kinetic Modeling. *J. Am. Chem. Soc.* **2015**, *137* (37), 12035−12044.
(71) Vequizo, J. J. M.; Matsunaga, H.; Ishiku, T.; Kamimura, S.; Ohno, T.; Yamakata, A. Trapping-Induced Enhancement of Photocatalytic Activity on Brookite TiO_2 Powders: Comparison with Anatase and Rutile TiO_2 Powders. *ACS Catal.* **2017**, *7* (4), 2644−2651.
(72) Yamakata, A.; Vequizo, J. J. M. Curious Behaviors of Photogenerated Electrons and Holes at the Defects on Anatase, Rutile, and Brookite TiO_2 Powders: A Review. *Journal of Photochemistry and Photobiology C: Photochemistry Reviews* **2019**, *40*, 234−243.
(73) Kohtani, S.; Kawashima, A.; Miyabe, H. Reactivity of Trapped and Accumulated Electrons in Titanium Dioxide Photocatalysis. *Catalysts* **2017**, *7* (10), 303.
(74) Fujishima, A.; Zhanng, X.; Tryk, D. TiO_2 Photocatalysis and Related Surface Phenomena. *Surf. Sci. Rep* **2008**, *63* (12), 515−582.
(75) Mills, A.; Le Hunte, S. An Overview of Semiconductor Photocatalysis. *J. Photochem. Photobiol. A Chem.* **1997**, *108* (1), 1−35.
(76) Schneider, J.; Matsuoka, M.; Takeuchi, M.; Zhang, J.; Horiuchi, Y.; Anpo, M.; Bahnemann, D. W. Understanding TiO_2 Photocatalysis: Mechanisms and Materials. *Chem. Rev.* **2014**, *114* (19), 9919−9986.
(77) Turkevich, J.; Fujita, Y. Methyl Radicals: Preparation and Stabilization. *Science (1979)* **1966**, *152* (3729), 1619−1621.
(78) Meyer, M.; Kerketta, S.; Hartman, R.; Kushner, M. J. CH_3 Radical Generation in Microplasmas for Up-Conversion of Methane. *J. Phys. Chem. A* **2024**, *128* (13), 2656−2671.
(79) Querebillo, C. J. A Review on Nano Ti-Based Oxides for Dark and Photocatalysis: From Photoinduced Processes to Bioimplant Applications. *Nanomaterials* **2023**, *13* (6), 982.
(80) Shetty, M.; Walton, A.; Gathmann, S. R.; Ardagh, M. A.; Gopeesingh, J.; Resasco, J.; Birol, T.; Zhang, Q.; Tsapatsis, M.; Vlachos, D. G.; Christopher, P.; Frisbie, C. D.; Abdelrahman, O. A.; Dauenhauer, P. J. The Catalytic Mechanics of Dynamic Surfaces: Stimulating Methods for Promoting Catalytic Resonance. *ACS Catal.* **2020**, *10* (21), 12666−12695.

https://doi.org/10.1021/acscatal.4c04312
ACS Catal. 2025, 15, 1195−1205

(81) Qi, J.; Resasco, J.; Robatjazi, H.; Alvarez, I. B.; Abdelrahman, O.; Dauenhauer, P.; Christopher, P. Dynamic Control of Elementary Step Energetics via Pulsed Illumination Enhances Photocatalysis on Metal Nanoparticles. *ACS Energy Lett.* **2020**, *5* (11), 3518−3525.
(82) Baldi, A.; Askes, S. H. C. Pulsed Photothermal Heterogeneous Catalysis. *ACS Catal.* **2023**, *13* (5), 3419−3432.
(83) Sordello, F.; Prozzi, M.; Hodoroaba, V.-D.; Radnik, J.; Pellegrino, F. Increasing the HER Efficiency of Photodeposited Metal Nanoparticles over TiO_2 Using Controlled Periodic Illumination. *J. Catal.* **2024**, *429*, No. 115215.
(84) Rahman, M. U.; Qazi, U. Y.; Hussain, T.; Nadeem, N.; Zahid, M.; Bhatti, H. N.; Shahid, I. Solar Driven Photocatalytic Degradation Potential of Novel Graphitic Carbon Nitride Based Nano Zero-Valent Iron Doped Bismuth Ferrite Ternary Composite. *Opt Mater. (Amst)* **2021**, *120*, No. 111408.
(85) Nadeem, F.; Zhang, H.; Tahir, N.; Zhang, Z.; Rani Singhania, R.; Shahzaib, M.; Ramzan, H.; Usman, M.; Ur Rahman, M.; Zhang, Q. Advances in the Catalyzed Photo-Fermentative Biohydrogen Production through Photo Nanocatalysts with the Potential of Selectivity, and Customization. *Bioresour. Technol.* **2023**, *382*, No. 129221.
(86) Iwaki, T. Studies of the Surface of Titanium Dioxide. Part 5.—Thermal Desorption of Hydrogen. *Journal of the Chemical Society, Faraday Transactions 1: Physical Chemistry in Condensed Phases* **1983**, *79* (1), 137.
(87) Rahimi, N.; Pax, R. A.; Gray, E. M. Mechanism of Hydrogen Modification of Titanium-Dioxide. *J. Alloys Compd.* **2020**, *815*, No. 152249.

https://doi.org/10.1021/acscatal.4c04312
ACS Catal. 2025, 15, 1195−1205